ACCSCIENCE PUBLISHING

International Journal of Bioprinting

RESEARCH ARTICLE

Optimization of 3D bioprinting of mouse preosteoblasts using nanofibrillated cellulose hydrogels

Na Li[1], LinGe Wang[2], Roxana Guillen De La Cruz[1]*, and Zhenyu Jason Zhang[1]*

[1] School of Chemical Engineering, University of Birmingham, Birmingham, UK

[2] South China Advanced Institute for Soft Matter Science and Technology, School of Emergent Soft Matter, Guangdong Provincial Key Laboratory of Functional and Intelligent Hybrid Materials and Devices, Guangdong Basic Research Centre of Excellence for Energy and Information Polymer Materials, South China University of Technology, Guangzhou, Guangdong, China

Abstract

Development and optimization of advanced bioink formulations for living tissue-engineered scaffolds remain a challenging task. Herein, a nanofibrillated cellulose (NFC)-composited gelatin methacryloyl (G)/alginate (A) formulation (G/A/NFC100) was prepared for 3D bioprinting of mouse preosteoblasts MC3T3-E1, whereby the G/A formulations with a mixed NFC/microfibrillated cellulose and without NFC were included for comparison. The rheological properties of G/A formulation were enhanced by the addition of NFC, as evidenced by a decreased viscosity index characterizing shear thinning behavior from 0.52 (G/A) to 0.19 (G/A/NFC100). To construct 3D scaffolds with excellent shape fidelity while minimizing shear damage to cells during extrusion, the bioprinting conditions of the formulations were optimized based on the parameter optimization index. The G/A/NFC100 scaffold printed at a printing speed of 2 mm/s and a dispensing pressure of 30 kPa from a 27-gauge nozzle displayed a high shape fidelity (printability index of 0.883). The mechanical stability of the crosslinked 20-layered G/A/NFC100 structures were demonstrated by three consecutive press-relax cycles. The successful bioprinting of mouse preosteoblasts using the G/A/NFC100 formulation translated into an increased cell viability (above 97.64%) up to 21 days post-bioprinting. These results emphasize the exceptional potential of NFC-composited G/A formulation for bioprinting of bone tissue analogues for biomedical applications. In addition, the long-term controlled release of ampicillin (67.42% after 72 h) by G/A/NFC100 scaffolds demonstrates the feasibility of utilizing porous cellulose fibers as drug-delivery carriers to enable multifunctionality in bone tissue repair.

Keywords: 3D bioprinting; Bioink formulation; Cell viability; Hydrogel; Nanofibrillated cellulose; Printability

***Corresponding authors:**
Roxana Guillen De La Cruz (rxg011@alumni.bham.ac.uk)

Zhenyu Jason Zhang (Z.J.Zhang@bham.ac.uk)

Citation: Li N, Wang L, De La Cruz RG, Zhang ZJ. Optimization of 3D bioprinting of mouse preosteoblasts using nanofibrillated cellulose hydrogels. *Int J Bioprint*. 2026;12(1):485-499. doi: 10.36922/IJB025420428

Received: October 18, 2025
1st revised: November 20, 2025
2nd revised: December 4, 2025
Accepted: December 8, 2025
Published online: December 16, 2025

1. Introduction

Three-dimensional (3D) bioprinting technology has emerged as a novel approach for fabricating biologically active 3D constructs in tissue engineering.[1-5] This cutting-edge

technique empowers the layer-by-layer deposition of diverse cell types, biomaterials, and biomolecules (collectively known as bioinks), facilitating the construction of predesigned, biologically functional 3D architectures.[6] By meticulously arranging the bioink in a sequential manner, 3D bioprinting overcomes the limitations of conventional scaffold fabrication methods, such as hydrogelation, freeze-drying, and electrospinning, thereby opening up new vistas in the realm of tissue-engineered substitute development.[7,8] Numerous 3D bioprinting technologies have emerged in the past decade,[9,10] among which extrusion-based bioprinting has gained the most popularity due to its operational practicality, high cell-encapsulation densities, and no exposure to high temperature or laser radiation.[11]

For extrusion bioprinting, the design of bioink formulation has been the focus of research due to the diverse performance requirements of 3D scaffolds for different tissues.[12] Natural polymer-based hydrogels, such as gelatin, collagen, fibroin, chitosan, sodium alginate, silk, and hyaluronic acid, can mimic the microenvironment of natural tissue and regulate cell fate at a high degree of hydration, making them the preferred materials for extrusion-based 3D bioprinting.[13,14] Traditional bioink formulations composed of gelatin (or gelatin methacryloyl) and alginate have been extensively studied due to their inherent biocompatibility and the complementary combination of photocrosslinkable and ionically crosslinkable networks.[15,16] However, this binary system still suffers from several intrinsic limitations, including insufficient rheological integrity for stable extrusion, inadequate mechanical robustness under highly hydrated conditions.[17,18] Cellulose, the most abundant natural polymers on the Earth,[19] has been shown to be suitable for a range of tissue engineering applications, e.g., wound healing, artificial blood vessels, soft tissue engineering, and bone engineering, due to its exceptional hydrophilicity, biocompatibility, and tunable physicochemical properties.[20,21] It is worth highlighting that nanocellulose, such as nanofibrillated cellulose (NFC) and cellulose nanocrystals (CNC), has been extensively used to address the shortcomings of conventional bioink formulations, such as poor processability, low gel strength, and rapid degradation after printing.[21-23] For example, NFC, as a reinforcing agent, was composited with a fucose-rich polysaccharide FucoPol to formulate a bioink with excellent rheological, mechanical, and biological characteristics for extrusion bioprinting of keratinocytes (HaCaT) and melanoma (A375) cells.[24] High cell viabilities (above 88%) up to 21 days post-bioprinting demonstrated the potential of such cellulose-composited formulation for the development of *in vitro* skin tissue analogues.

In our previous study, both NFC and microfibrillated cellulose (MFC), were introduced to gelatin methacryloyl (G)/alginate (A) system as mechanical strengthening agents.[25] By characterizing the multiscale mechanical properties of cellulose-composited ion–covalent entanglement (ICE) G/A hydrogels, new mechanical reinforcement mechanisms were demonstrated. Controlling the ratio of MFC to NFC can modulate Young's modulus of the hydrogel system to broaden its application range. We also found that adjusting the incorporation concentration of pure MFC in the G/A formulation can balance the rheological properties, mechanical properties, and a range of biological behaviors of the formulation.[26] Building up the capability to control the mechanical properties of cellulose-composited hydrogel, the optimization of extrusion-based 3D bioprinting of mouse preosteoblasts-encapsulated NFC-composited G/A formulations was investigated in this work according to the workflow for the bioink development proposed by Gatenholm *et al.*[27] We sequentially evaluated the rheology, printability, crosslinking stability, sterility, bioprinting, and cell proliferation of the cellulose-composited hydrogel, with a particular emphasis on its potential as a drug delivery vehicle.

2. Materials and methods

2.1. Materials

Gelatin from porcine skin (gel strength 300, type A), methacrylic anhydride (MA, 94%), sodium alginate from *Macrocystis pyrifera* (A, mannuronate/guluronate ratio of 2.03, M_v of 478.44 kDa), 2-hydroxy-4′-(2-hydroxyethoxy)-2-methylpropiophenone (Irgacure 2959), ampicillin sodium salt (AMP), Miller Luria–Bertani (LB) broth, and tryptic soy broth (TSB) were purchased from Sigma-Aldrich (Somerset, UK). Microfibrillated cellulose (MFC) suspension (0.7 wt%, purity of 99.9% cellulose, negative surface zeta-potential of −24.0 ± 0.5 mV at pH 5.7, cellulose fibrils with an average diameter of 0.3–2 μm[25]), prepared by mechanical grinding of softwood bleached Kraft pine pulp, was kindly donated by FiberLean Technologies Ltd (Par, UK). Nanofibrillated cellulose (NFC) suspension (3 wt%, purity of 85% cellulose, 12% hemicellulose, and 3% lignin, negative surface zeta-potential of −15.0 ± 0.4 mV at pH 4.2, cellulose fibrils with an average diameter of 30–100 nm[25]), prepared by high pressure homogenization of bleached softwood Kraft pulp, was purchased from Cellulose Lab (Canada) and diluted to 1 wt% for use. Calcium chloride ($CaCl_2$), sodium hydroxide (NaOH), phosphate-buffered saline (PBS) tablets, and nutrient agar were purchased from Fisher Scientific (Loughborough, UK). Calcium chloride was prepared as a 2% solution and NaOH was prepared as a 1 M solution for use.

Mouse preosteoblasts MC3T3-E1 Subclone 4 cells (ATCC-2593) were purchased from LGC standards (Middlesex, UK). Alpha Minimum Essential Medium (αMEM) with *L*-glutamine, fetal bovine serum (FBS), penicillin–streptomycin (10,000 U/mL), trypsin–EDTA (0.05%), trypan blue (0.4%), Dulbecco's phosphate-buffered saline (dPBS, 1×) with and without calcium and magnesium, and collagenase type II were purchased from Gibco, Thermo Fisher Scientific (Loughborough, UK). LIVE/DEAD Viability/Cytotoxicity Kit for mammalian cells was obtained from Invitrogen, Thermo Fisher Scientific (Loughborough, UK). Basal culture media of MC3T3-E1 cells comprised αMEM, 10% FBS, and 1% penicillin–streptomycin. Collagenase type II was dissolved in 1× dPBS to prepare a stock solution (50,000 U/mL), followed by sterilization using 0.2 μm PES syringe filter. The stock solution of collagenase type II was stored at −18°C until use.

Strains of *Escherichia coli* (*E. coli*; MG1655, ATCC 47076) and *Staphylococcus aureus* (*S. aureus*; ATCC 29213) were obtained from the School of Biochemical Engineering, University of Birmingham, UK. Nutrient agar, PBS tablets, LB broth, and TSB broth were all dissolved in deionized water with appropriate concentrations and autoclaved at 121°C for 20 min following the manufacturer's protocol.

2.2. Preparation of cell-free bioink formulations

Gelatin methacryloyl (G, 80% methacrylated) was synthesized by gelatin and MA, as described in our previous study.[25] MFC and NFC in PBS were mixed and homogenized at five different volume ratios of 0:100, 25:75, 50:50, 75:25, and 100:0, separately. The corresponding cellulose suspensions were named NFC100, MFC25/NFC75, MFC50/NFC50, MFC75/NFC25, and MFC100. Cell-free cellulose-composited G/A bioink was formulated by adding 7.5 w/v% G, 2 w/v% A, and 0.35 w/v% Irgacure 2959 to the above five types of cellulose suspensions, followed by homogenization at room temperature (19°C) and then heating in a 50°C water bath for 12 h until sample G and A reached a dissolution equilibrium. The resulting product was centrifuged at 500 rpm for 1 min to remove air bubbles and stored at room temperature for use. The five different bioink formulations were named G/A/NFC100, G/A/MFC25/NFC75, G/A/MFC50/NFC50, G/A/MFC75/NFC25, and G/A/MFC100, respectively.

2.3. Rheological characterization

Rheological measurement of bioink formulations was carried out using a rheometer (Discovery HR-1, TA Instrument, UK), with a Peltier cone-plate measurement geometry (diameter of 40 mm, cone angle of 4°, truncation gap of 112 μm). Samples were subjected to a shear rate (γ) sweep ranging from 0.01 to 100 s^{-1} while the shear stress (σ) was recorded. Power-law flow model was used to analyze the flow behavior of samples:

$$\sigma = k_{PL}\gamma^{n_f} \quad \text{(I)}$$

where k_{PL} and n_f are flow consistency index and viscosity index, respectively. The rapid recoverability of viscosity for bioink formulations postextrusion was assessed by a dedicated peak hold program, with which the shear rate was set to 1 s^{-1} for 60 s initially, increased to 300 s^{-1} for 5 s to replicate the extrusion process, and finally reduced to 0.1 s^{-1} for 235 s. Furthermore, a strain cycle program was applied to track the recoverability of storage modulus (*G'*) and loss modulus (*G"*) upon four cycles of high strain (100%) for 150 s and low strain (1%) for 150 s at a frequency of 1 Hz. The sample was allowed to stabilize for 5 s at each transition between high and low strain. The testing temperature was set at 25°C. The sample was placed on the geometry plate for 3 min before each test to ensure a uniform temperature. Every type of measurement was repeated in triplicate.

2.4. 3D printing

The printability of cell-free bioink formulations was assessed by a nozzle-based pneumatic extrusion bioprinter (RegenHU, 3D Discovery, Switzerland). The effects of printing parameters, including dispensing pressure (P), printing speed, and nozzle gauge (G_N), on printing accuracy and shear stress were investigated by measuring the width of extruded filament line (W_L). Parameter optimization index (POI) was introduced to determine the optimal printing conditions of formulations and is expressed as follows:

$$POI_i = \frac{1}{W_L \cdot P \cdot G_N} \quad \text{(II)}$$

$$POI = \frac{POI_i}{POI_{MAX,n}} \quad \text{(III)}$$

where POI_i stands for POI in an individual set of parameters and $POI_{MAX,n}$ denotes the maximum POI_i over the total range of parameter combinations n. Therefore, the value of POI is between 0 (the worst) and 1 (the best).[28,29] The dispensing pressure was adjusted in the range of 20–60 kPa and printing speed was chosen from 2 to 74 mm/s. The predicted widths of the filament provided by the bioprinting software are 0.47 and 0.23 mm when being extruded from 22- (22G) and 27-gauge (27G) nozzles, respectively. Images of filaments at different printing parameters were captured

and analyzed using Image J software (National Institutes of Health, USA). At least ten different positions on the filament were selected to calculate the averaged width of the filament.

The formulated bioinks were subsequently printed to two-dimensional (2D) lattices (side of 20 mm, line space of 4 mm, grids of 5 × 5) at the optimal printing conditions to investigate 2D printability using printability index (*Pr*):

$$Pr = \frac{L^2}{16A} \quad \text{(IV)}$$

where L and A are the perimeter and area of one grid constructed, respectively. Bioink formulations that produced square grids in the printed lattice have the optimum *Pr* of 1, while samples with circular grids due to interlayer fusion showed the worst *Pr* of $\pi/4$.[30]

Stability of the crosslinked scaffolds was evaluated by constructing a 20-layered structure with three different shapes: an 8 mm square, a 9 mm pentagram, and a 10 mm-diameter tube. Formulated G/A/NFC100 was dispensed by a 22G nozzle at a printing speed of 22 mm/s and dispensing pressure of 25 kPa. These structures were subsequently crosslinked by exposing to a ultraviolet (UV) source (OmniCure S2000 Spot UV Curing System, wavelength of 365 nm, iris setting of 70%, working distance of 2 cm) for 3 min, followed by immersion in a 2% $CaCl_2$ solution for 3 min. These hollow structures were pressed manually, of which the shape recovery process was recorded.

2.5. Swelling

The formulated bioinks were placed in a customized elastomer mould, followed by UV irradiating for 3 min and submerging in 2% $CaCl_2$ for 12 h at room temperature to allow double crosslinking. Cellulose-composited ICE G/A hydrogel discs with a thickness of 4 mm and a diameter of 12 mm were immersed in PBS solution for 24 h to remove unreacted Irgacure 2959 and Ca^{2+}. Such hydrogel discs were freeze-dried to measure their initial dry mass (W_{dry}), and subsequently immersed in deionized water for 48 h at room temperature. Equilibrium hydration degree (EHD) of the hydrogel disc was estimated using the wet mass after 48 h swelling ($W_{wet,48\,h}$) based on the following equation:

$$EHD(\%) = \frac{W_{wet,48h} - W_{dry}}{W_{wet,48h}} \times 100 \quad \text{(V)}$$

2.6. Biodegradation characterization

Each dried hydrogel disc was immersed in 1 mL of 1× dPBS containing 5 U/mL collagenase type II and kept at 37°C. The enzymatic biodegradation solution was replaced every 2 days. After 1, 3, 7, and 10 days, the remaining hydrogel disc was lyophilized and weighed, based on which the biodegradation rate (*BDR*) was calculated according to the equation below:

$$BDR(\%) = \frac{W_{dry} - W_n}{W_{dry}} \times 100 \quad \text{(VI)}$$

where W_n is the remaining dry mass of the samples after biodegradation of n day.

2.7. Morphological characterization

Changes in the morphology of the hydrogel during biodegradation were recorded by scanning electron microscopy (SEM; XL-30 field emission, Philips, USA). Freeze-dried hydrogel discs were coated with a gold layer with a thickness of approximately 20 nm prior to the SEM measurement. Micro-computed tomography (μCT; SkyScan 1172, Bruker, Germany) was used to investigate the structural characteristics of the freeze-dried hydrogel discs in 360° at a rotation step of 0.4°. The resulting 2D projection images of specimens were reconstructed by NRecon and organized to 3D images in CT Analyzer (CTAn; Bruker, Germany) software program to obtain the porosity and pore size distribution of the sample.

2.8. Bioprinting

Formulation component G, A, and Irgacure 2959 were dissolved in an autoclaved NFC suspension under the sterile environment, followed by homogenization, water bath, and degassing. The resulting sterile G/A/NFC100 formulation was gently mixed with mouse preosteoblasts MC3T3-E1 Subclone 4 (passages 6–9). The cell-containing bioink formulation with a density of 1.56×10^6 cells/mL was loaded into the bioprinter and extruded with a 27G nozzle at a print speed of 2 mm/s and a dispensing pressure of 25 kPa. The resulting scaffolds with side length of 10 mm and layer numbers of 4–6 were exposed to UV radiation for 10 and 15 s, respectively, and immersed in 2% $CaCl_2$ subsequently for 5 min. Cell-encapsulated scaffolds were cultured in a humidified incubator at 37°C with 5% CO_2, and cell culture medium was changed every 2 days.

2.9. Live/dead assay

Cell viability in 4- and 6-layered scaffolds was measured using the Live/Dead assay following the manufacturer's protocol. Calcein-AM and ethidium homodimer-1 were diluted in sterile dPBS and mixed thoroughly. At each time point, the scaffold sample was incubated in 1 mL of staining solution containing 1 μL/mL calcein-AM and 4 μL/mL ethidium homodimer-1 at 37°C with 5% CO_2 for 20 min. Once the staining reagent was gently aspirated, the scaffold was washed once with dPBS to minimize any

potential background signal. The cell-loaded scaffolds were imaged using a confocal laser scanning microscope (Zeiss LSM780, Carl Zeiss Microscopy, US). ImageJ was then used to process the Z-stack images of the cells and to perform live/dead cell counts.

2.10. Drug loading

Ampicillin was used as a model drug to study the controlled drug release profile of hydrogels in this work. Preweighted dried hydrogel discs were immersed in 50 mL standard solution of ampicillin (100 μg/mL), followed by incubation at 20°C with a continuous agitation at 100 rpm. At scheduled time intervals, free ampicillin of 1 mL was aspirated, and the absorbance was read at 220 nm immediately using a UV/Vis spectrometer (BiochromLibraS12, Cambridge, UK). The standard calibration curve of ampicillin was obtained before the test. The withdrawn liquid was replaced with an equal volume of fresh sterile PBS. The drug loading capacity (*LC*, measured as mg/g) after 24 h was determined following the equation below[31]:

$$LC\left(\frac{mg}{g}\right)=\frac{W_{\mathrm{Amp,T}}-W_{\mathrm{Amp,F}}}{W_{\mathrm{dry}}} \quad \text{(VII)}$$

where $W_{\mathrm{Amp,T}}$ (mg) is the total ampicillin mass, while $W_{\mathrm{Amp,F}}$ (mg) represents the free mass of ampicillin after 24 h. In this work, the ampicillin-loaded hydrogel specimens were named as G/A-AMP and G/A/NFC100-AMP.

2.11. Drug release

Ampicillin-loaded hydrogels were immersed in 50 mL of sterile PBS at 20°C, shaken continuously at 80 rpm. At predetermined time intervals, 1 mL release medium was pipetted and replaced with same amount of fresh PBS solution. The amount of cumulative released ampicillin ($W_{\mathrm{Amp,R}}$) was recorded using a spectrometer. The cumulative release (*CR*) of ampicillin was estimated by the following equation:

$$CR(\%)=\frac{W_{\mathrm{Amp,R}}}{W_{\mathrm{Amp,T}}-W_{\mathrm{Amp,F}}}\times 100 \quad \text{(VIII)}$$

The measurement was terminated when the absorbance of the release medium reached equilibrium. The first 60% release of ampicillin was logarithmically fitted based on the power-law model:

$$\frac{M_t}{M_\infty}=kt^{n_r} \quad \text{(IX)}$$

where M_t and M_∞ are the cumulative release amount of the drug at time *t* and the total amount of drug that can be released, respectively; *k* is the release rate constant.[32] More importantly, the release index (n_r) is used to characterize the drug release mechanism. For cylindrical polymer release system applicable to this work, $n_r \leq 0.45$ indicates a Fickian diffusion-controlled release (case I transport), while n_r of 0.89 (case II transport) means that the drug is released at a constant rate and independent of drug concentration and time. In most cases reported in the literature, n_r lies between 0.45 and 0.89, suggesting that the drug release is governed by a combination of diffusion and other complex factors where the release mechanism is anomalous transport. Only in rare cases, such as when the polymer matrix is severely modified, the release index is greater than 0.89 and a super case II diffusion occurs.[33,34]

2.11. Agar disc diffusion assay

E. coli was incubated in LB broth while *S. aureus* in TSB medium overnight at 37°C with a constant shaking at 150 rpm. The overnight grown bacterial cultures were pelleted, washed twice, and resuspended in the corresponding growth media to achieve an optical density (OD) at 600 nm of 0.5 AU. G/A-AMP and G/A/NFC100-AMP hydrogel discs were filled into agar plate wells. Bacterial cultures of 150 μL were distributed uniformly across the agar plate and statically incubated at 30°C for *E. coli* and 37°C for *S. aureus* for 24 h, respectively. The inhibitory zones for bacterial growth were subsequently measured. All samples were transferred from the day-1 plates into freshly inoculated agar plates and subsequently incubated for an additional 24 h followed by the same measurements. This procedure was repeated, and the inhibitory results were recorded after a total incubation period of 3 days. Both positive (100 μg/mL ampicillin-loaded filter paper discs with 13 mm diameter) and negative control (G/A and G/A/NFC100) procedures were carried out in accordance with the same protocol. Every sample against bacterial strains was subjected to three independent replicates.

2.12. Statistical analysis

The results from quantitative experiments were analyzed in OriginPro 2022 (OriginLab, USA) and expressed as mean ± standard deviation ($n \geq 3$). Significant differences were determined using one-way analysis of variance (ANOVA) followed by Tukey's post hoc test for pairwise comparisons. Statistical significance was determined at the 0.05 level. The *p*-values labeled in all figures are $^{*}p \leq 0.05$, $^{**}p \leq 0.01$, and $^{***}p \leq 0.001$, respectively.

3. Results and discussion

3.1. Rheological properties

Viscosity of the bioink plays a pivotal role in 3D bioprinting. Because the viscoelastic behavior of each formulation is influenced by the intrinsic properties of the components applied, suitable viscosity range of bioink formulations

for extrusion bioprinters covers a broad range from 30 to 6 × 10^7 mPa s^{-1}.[35] For a given formulation, it is crucial to consider the upper limit of viscosity (principle of not clogging the nozzle), the lower limit (criterion for forming connected filaments rather than droplets), and the change in viscosity during the extrusion process for a successful printing execution while minimizing the impact of the shear on the encapsulated cells.[36] In this work, flow behaviors of the mixed cellulose suspensions were characterized (Figure 1A) prior to investigating the change in viscosity of formulated bioinks as a function of the shear rate. With an increased shear rate from 10^{-2} to 10^2 s^{-1}, viscosity of cellulose suspensions was found to decrease by five orders of magnitude within above viscosity range of 30–6 × 10^7 mPa s^{-1}, exhibiting an excellent shear-thinning behavior. Our previous study shows that the viscosity of the G/A formulation decreases from 40.4 to 2.1 Pa·s in the same shear rate range and the corresponding viscosity index is 0.52.[26] However, once the cellulose fibres were introduced to the G/A formulation, the viscosity range of the bioink formulations is expanded significantly to three orders of magnitude (about 8,000 to 7 Pa·s) under the same shear rate range (Figure 1B). The rheological behavior of all five samples was found to follow power law model (R^2 of greater than 0.99) with n_f numbers of approximately 0.2 (Figure 1C), which is in a good agreement with the shear thinning properties previously observed for nanocellulose system by other research groups.[37,38] The shear-thinning behavior of the cellulose-composited G/A formulations confirms that the polymeric constituents of the bioink formulation could be aligned in the direction of the shear-induced flow since the interactions between them were readily disrupted by the shear forces. It is worth noting that neither the differences in cellulose fiber size nor the NFC/MFC ratios in bioink formulations has a notable impact on the shear-thinning behavior of the cellulose composited G/A bioink.

The fast self-healing or recovery properties of the bioink post extrusion were characterized by peak hold (Figure 1D) and dynamic low-high strain tests (Figure 1E). The viscosity of all cellulose-composited G/A formulations

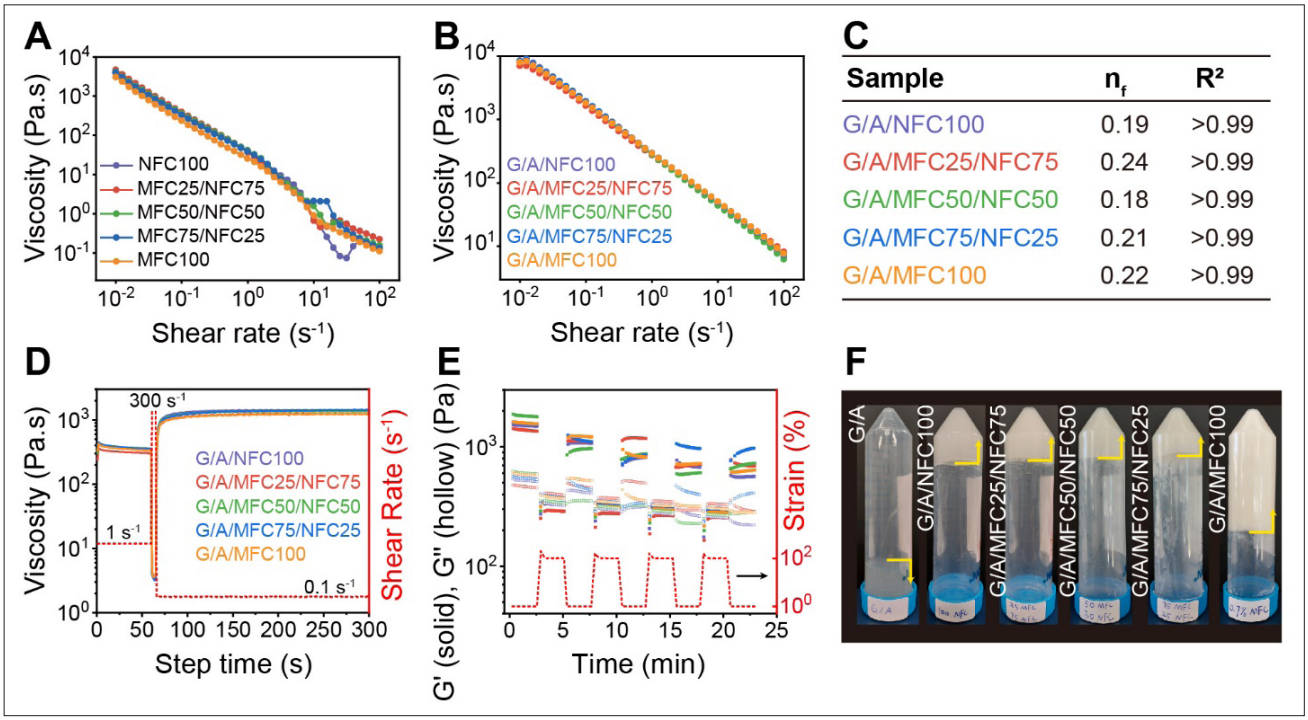

Figure 1. Rheological properties of G/A formulation enhanced by fibrillated cellulose. (A) Viscosity of cellulose suspension NFC100, MFC25/NFC75, MFC50/NFC50, MFC75/NFC25, and MFC100 as a function of shear rate. (B) Viscosity of bioink formulation G/A/NFC100, G/A/MFC25/NFC75, G/A/MFC50/NFC50, G/A/MFC75/NFC25, and G/A/MFC100 as a function of shear rate. (C) Power law viscosity index (n_f) of cellulose incorporated G/A formulations. Both MFC and NFC can improve the shear-thinning behavior of G/A formulation. (D) The viscosity response of cellulose-composited G/A bioinks to sudden increase in shear rate to 300 s^{-1} at 60 s and decrease to 0.1 s^{-1} at 65 s, respectively. (E) Changes of storage modulus (*G'* in solid points) and loss modulus (*G"* in hollow points) for formulations in dynamic strain cycle alternating 1% for 150 s and 100% strain for 150 s. (F) Cellulose-composited G/A formulations and the benchmark are inverted for 1 h. The benchmark G/A flows to the top of the sample tube, while cellulose-composited G/A formulations remain in the initial position, indicating the gel state of the formulations. Abbreviations: G/A, Gelatin methacryloyl/alginate; MFC, Microfibrillated cellulose; NFC, Nanofibrillated cellulose.

immediately decrease to approximately 4 Pa·s when the shear rate rises from 1 to 300 s^{-1} but increase to nearly 1050 Pa·s in just 8 s responding to the sudden drop of shear rate to 0.1 s^{-1} (Figure 1D). Moreover, the formulations display the characteristic rheological behavior of a gel ($G' > G''$) at low strains (1%). However, G' drastically decreases, suggesting a sol state is formed ($G'' > G'$), once a high strain (100%) is applied, following which a gel-like behavior is observed upon the introduction of low strain. Such recovery behavior can be observed after four high-low strain repeated cycles (Figure 1E). The results align with our previous work concerning MFC-composited G/A formulation,[26] and further evidence the high recovery properties of pure NFC-composited and hybrid cellulose-composited G/A formulations.

Figure 1F and Figure S1 show the macroscopic gel or sol behavior with visual evidence by inverting the centrifuge tubes containing the bioink formulation after 1 h. In both the single-component and binary systems, all samples migrated to the opposite end of the tube, exhibiting a freely flowing, sol-like behavior. This observation indicates that the physical entanglement among the components in these one- and two-component formulations is too weak to achieve the minimum viscosity required for maintaining continuous filaments after extrusion. In contrast, any ternary formulation of G/A containing cellulose remained in place, demonstrating that all three components are indispensable; the mutual entanglement among them yields a sufficiently high viscosity that drives the system into a gel-like state. Such gel-like behavior not only helps maintain a stable and homogeneous formulation prior to printing but also enables the extruded filaments to retain their shape after deposition.

3.2. Printability analysis of formulations

To determine the optimal printing conditions for the bioink formulations, the effects of dispensing pressure, print speed, and nozzle size on the precision of extruded filaments were studied. Figure S2 shows the acquired images and corresponding line widths of filaments formed by G/A/MFC100 formulation using a 27G nozzle as a function of dispensing pressures and print speeds. The gray area is the printable area. Both Figure S2 and Figure 2A show that the line width decreases exponentially as the printing speed increases under a constant dispensing pressure. Figure 2B reveals that the line width increases linearly with the rise of dispensing pressure at a constant printing speed. It is worth highlighting that the filament exhibits the thinnest line width of 0.49 mm when the print speed is 24 mm/s and the dispensing pressure is 55 kPa. Taking consideration of the damage to the encapsulated cells by shear stress during the extrusion process and the accuracy of printing, Figure 2C shows that *POI* has a maximum value with a line width of 0.5 mm when the print speed is 2 mm/s and the dispensing pressure is 30 kPa, which is the optimal printing condition for such formulation when using a 27G nozzle.

The continuity of the filament is observed to be seriously damaged, so-called under-extrusion, when the dispensing pressure is less than 30 kPa (pink area), or the print speed is too fast (yellow zone), as shown outside the gray printable area of Figure S2. If the bioink formulation is extruded at a print speed of less than 2 mm/s at a dispensing pressure of 30–40 kPa, especially when constructing larger-sized scaffolds, long printing time would naturally cause water evaporation in the scaffold, resulting in a failed construction (orange region). When the print speed is less than 2 mm/s and the distribution pressure is greater than 45 kPa, the resolution of the filament drops sharply, resulting in over-extrusion (blue area). In addition, distribution pressure should be adjusted by taking serious consideration of the impact of shear force on cell viability (green zone).

When a 22G nozzle was used to extrude G/A/MFC100 formulation, the printable area (gray region) was found to be greater than that when using a 27G nozzle (Figure S3). It is clear that the increased nozzle inner diameter (200–410 μm) allows the 3D printer to dispense filament at an increased print speeds for high resolution. The influence of print speed and dispensing pressure on filament line width (Figure 2D and E) is consistent with the findings when using a 27G nozzle. Although the thinnest line width (0.67 mm) was produced at a print speed of 60 mm/s and a dispensing pressure of 40 kPa (Figure S3), the optimal printing condition was identified as 22 mm/s and 25 kPa, resulting in a line width of 0.85 mm, once taking consideration of the maximum *POI* value (Figure 2F).

It can be concluded that the printing resolution and printability index (0.892) of G/A/MFC100 are the highest and the degree of interlayer fusion of G/A/MFC100 is the lowest among all three samples studied (Figure 3A) when bioink formulation G/A, G/A/NFC100, and G/A/MFC100 were printed to 2D lattice under the optimal printing condition of G/A/MFC100. The internal lattice of G/A/NFC100 scaffold also tends to be square, as quantified by *Pr* of 0.883, confirming that G/A/MFC100 and G/A/NFC100 show a very similar printability.

The shape fidelity of NFC-composited G/A bioink formulation G/A/NFC100 was evaluated by building a 20-layered construct with different shapes. Since the difference in *Pr* between G/A/NFC100 and G/A/MFC100 is not significant ($p > 0.05$), the optimal printing condition of G/A/MFC100 (printing speed of 22 mm/s, dispensing pressure of 25 kPa, 22G nozzle) was used to extrude

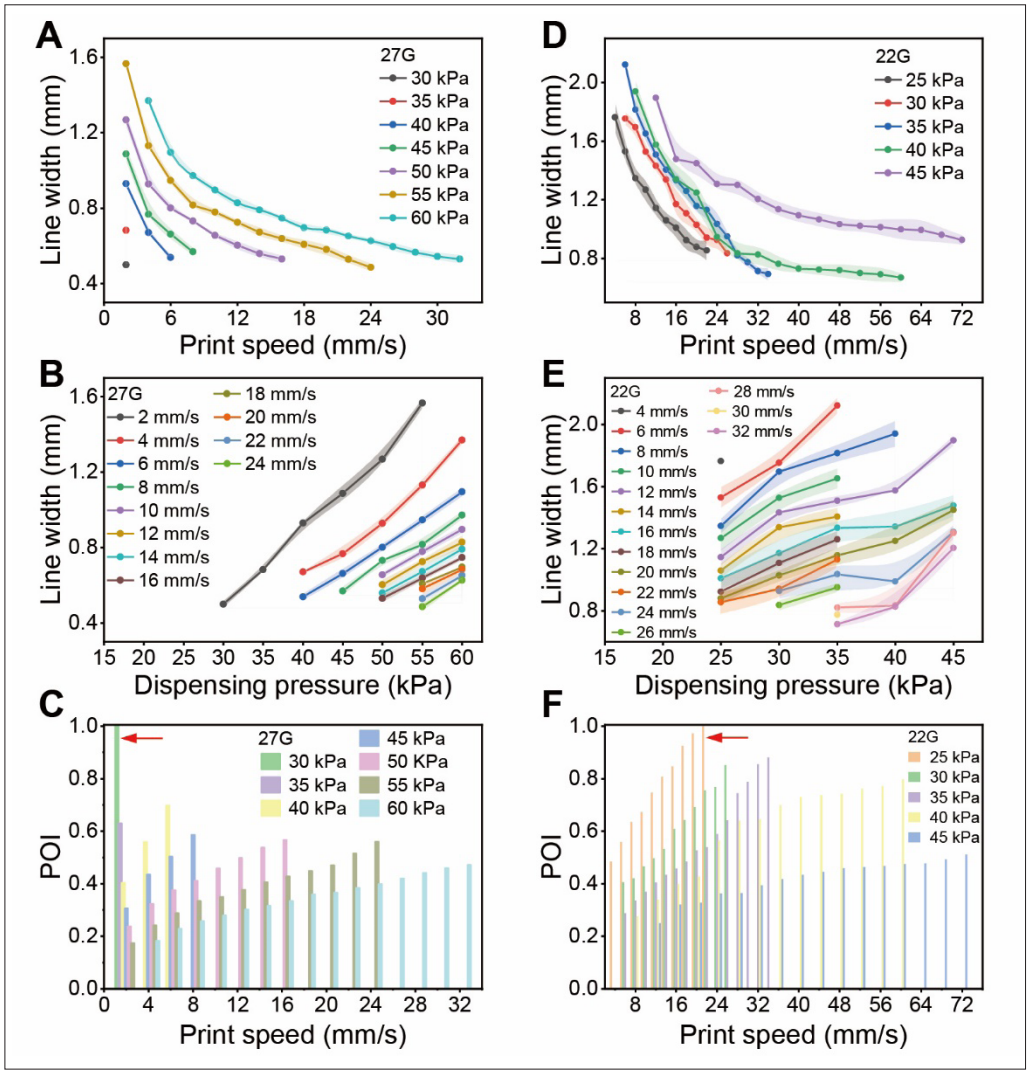

Figure 2. The effects of dispensing pressure, print speed, and nozzle size on the precision of extruded filaments. (A,B) Line width of G/A/MFC100 filament extruded from 27G nozzle as a function of print speed at constant dispensing pressures (A) and dispensing pressure at constant print speeds (B). (C) Comparison of *POI* when G/A/MFC100 was extruded from 27G nozzle, displaying that the optimal printing condition is at 2 mm/s print speed and 30 kPa dispensing pressure. (D,E) Line width of G/A/MFC100 filament extruded from 22G nozzle as a function of print speed at constant dispensing pressures (D) and dispensing pressure at constant print speeds (E). (F) Comparison of *POI* when G/A/MFC100 was extruded from 22G nozzle, demonstrating the optimal printing condition at 22 mm/s print speed and 25 kPa dispensing pressure. Abbreviations: G/A, Gelatin methacryloyl/alginate; MFC, Microfibrillated cellulose; POI, Parameter optimization index.

G/A/NFC100 layer by layer. Figure 3B and C displays the 3D model design and top views of the corresponding constructs, respectively. It is obvious that the side length of the square structure (8 mm) and the length between the two nonadjacent vertices of the five-pointed star (9 mm) are consistent with their corresponding lengths in the design, demonstrating the excellent shape fidelity of NFC-composited ICE hydrogel scaffolds. However, when the tubular structure was constructed, the diameter of the structure is slightly greater than the designed length (10 mm) by approximately 1 mm, indicating that the printing resolution of the G/A/NFC100 formulation needs further improvement. It is worth noting that the G/A/MFC100 formulation was selected as the representative system in determining the optimal printing conditions. Although G/A/MFC100 and G/A/NFC100 exhibit no significant differences in rheological behavior, the latter is intended for printing more complex scaffold geometries in the subsequent stages. Therefore, the current printing parameters serve as a baseline, and the established relationships between filament resolution, printing speed, and dispensing pressure will guide the refinement of the

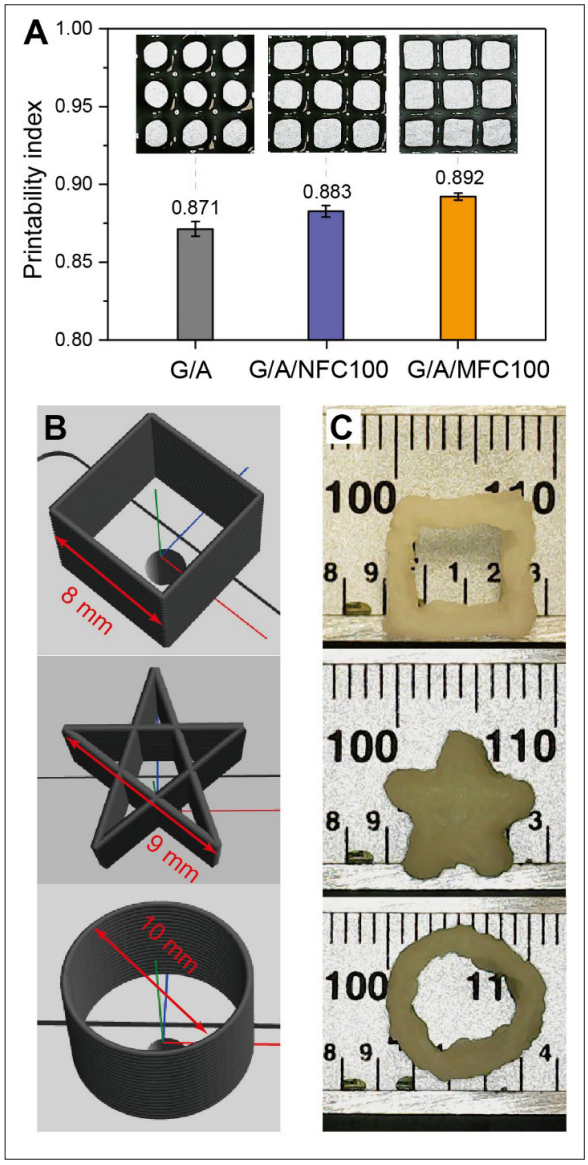

Figure 3. The printability of G/A/NFC100 formulation and the shape fidelity of corresponding constructs. (A) Printability indices and images of scaffolds extruded with G/A, G/A/NFC100, and G/A/MFC100 under the same printing condition (print speed of 2 mm/s, dispensing pressure of 30 kPa, and 27G nozzle). (B) Models and (C) corresponding 20-layered printed structures of G/A/NFC100 at a printing speed of 22 mm/s and a dispensing pressure of 25 kPa using a 22G nozzle. Abbreviations: G/A, Gelatin methacryloyl/alginate; MFC, Microfibrillated cellulose; NFC, Nanofibrillated cellulose.

optimal printing window for G/A/NFC100 to enable the fabrication of high-resolution constructs.

In addition, by performing three consecutive press-relax cycles from the sides of these three constructs using a tweezer (Videos S1, S2, and S3), we showed that the shape of the constructs changed accordingly, but returned to the initial state after the last relax fully, proving the mechanical stability of crosslinked interlayers and excellent elasticity of the crosslinked body. As demonstrated in our previous work,[25] this mechanical stability arises from the synergistic interactions within the ion–covalent interpenetrating dual network formed by gelatin methacryloyl and sodium alginate, further reinforced by the additional cooperation of NFC with this dual-network structure.

3.3. The effect of cellulose on equilibrium hydration degree and enzymatic biodegradation behavior of G/A ICE hydrogel

Previous experiments by the authors show that the swelling ratio of the dried hydrogel G/A/MFC100 reaches equilibrium after 1 day of immersion in water and remains

constant for 10 days.[26] In this work, the effects of NFC and hybrid cellulose on the *EHD* of G/A ICE hydrogels were evaluated based on the same protocol, of which the results are shown in Figure 4A**.** G/A/NFC100 and hybrid cellulose-composited G/A ICE hydrogels (G/A/MFC25/NFC75, G/A/MFC50/NFC50, G/A/MFC75/NFC25) have no significant differences in *EHD* with G/A/MFC100 ($p > 0.05$) and all remain around 87%, indicating that the size of fibrillated fiber does not have a noticeable effect on the water content of the hydrogel.

The effect of NFC on the enzymatic biodegradation profile of G/A ICE hydrogel in dPBS containing 5 U/mL collagenase type II was investigated. As shown in Figure 4B and Figure S4, *BDRs* of G/A/NFC100 after 3, 7, and 12 days are 5.56%, 37.08%, and 50.99%, respectively, slightly faster than that of G/A/MFC100 (3.21%, 31.77%, and 45.52% after 3, 7, and 12 days, respectively). In contrast, *BDR* of G/A reaches 62.55% after 7 days, and the G/A sample fully biodegrades over 12 days.[26] Hence, the incorporation of fibrillated cellulose can significantly slow down the chain breakage of gelatin methacryloyl and consequently prolong the biodegradation process of G/A ICE hydrogel. This result is supported by the porosity data of the materials (60.85% of G/A, 41.9% of G/A/MFC, and 43.19% G/A/NFC100) reported in our previous studies.[25] The entanglement between fibrillated cellulose and the ICE network enhances the crosslinking density and reduces the porosity of the system, and thus increases the diffusion resistance of collagenase type II. In addition, the morphology and pore size distribution of the G/A/NFC100 hydrogel were captured by SEM (Figure 4C, D, and E) and μCT (Figure 4F) before biodegradation, after 3 and 7 days upon initiation of the biodegradation. Although the biodegradation behavior of G/A/NFC100 results in an increased pore size and an expanded pore size distribution, G/A/NFC100 retains an internally connected pore structure after 7 days of biodegradation, which is consistent with the morphological changes of G/A/MFC100 during the biodegradation process, but is in obvious contrast to those of G/A (characterized by pore wall cracking and nonconnectivity).[26] Connected pore structure of G/A/fibrillated cellulose hydrogel during *in vivo* and *in vitro* culturing process is important for the ordered transportation of nutrients and metabolic wastes of cells within the scaffold.

3.4. Bioprinting of cell-laden scaffolds and cell viability after bioprinting

The biocompatibility of G/A/NFC100 was studied by printing cell-encapsulated scaffolds and culturing them continuously for 21 days. As shown in Figure 4G–H and Figure S5, MC3T3-E1 are evenly distributed in the scaffold, and the cell viabilities in the 4- and 6-layered scaffolds gradually increase from 67.89% to 96.25% and from 79.83% to 97.64%, respectively, within the first 10 days. After 14 days in culture, cells started elongating along the inner structure of the scaffold. Furthermore, cells proliferated significantly after 21 days, confirming the cytocompatibility of G/A/NFC100. Moreover, it was found that the growth profiles of MC3T3-E1 within G/A/NFC100 and G/A/MFC100[26] scaffolds are consistent, indicating that despite the size differences between NFC and MFC, both types of fibrillated cellulose can protect cells from shear damage during extrusion printing and do not affect the growth kinetics of encapsulated MC3T3-E1 over the 21-day *in vitro* culture period. On the other hand, the cell-attachment properties of gelatin have been widely reported[39] and our experimental results further illustrate that the growth process of cells in the scaffold was relatively slow before adhesion occurred, but the life activities of the cells can be significantly accelerated after adhesion to gelatin. Furthermore, changes in the pore structure of the cell-encapsulated G/A/NFC100 scaffolds were captured over 21 days of culture (Figure 4I). Compared with the samples cultured for 7 days, the pore sizes of the 4- and 6-layered scaffolds cultured for 21 days were found to increase, which can be attributed to the natural degradation caused by the decreased crosslinking density of the scaffold and the biodegradation associated with cellular activities. It is believed that the increasing pore size of the scaffold and the growth of cells can offer complementary advantages, forming a favorable environment for tissue remodeling.

3.5. Drug release profile and effects of NFC on functions of ampicillin in hydrogels

According to **Equation (VII)**, the saturated loading capacities of the dried hydrogel disc G/A and G/A/NFC100 after 24 h of immersion in standard ampicillin solution are 7.34 and 8.12 mg/g, respectively, demonstrating the ability of NFC to increase the drug loading of G/A. Additionally, NFC incorporation was found to significantly alter the drug release profile of G/A-AMP when ampicillin was released from hydrogel samples, as shown in Figure 5A. Based on the 50% cumulative release of ampicillin, we found that NFC could prolong the drug release from G/A-AMP from 4.92 h to 24–48 h. Moreover, the cumulative release of ampicillin from G/A/NFC100-AMP was 67.42% until 72 h, higher than that of G/A/MFC100-AMP (43.75%) due to the difference in porosities (Figure S6A). Yet, both G/A/NFC100-AMP and G/A/MFC100-AMP displayed an initial mild release in the first 6 h followed by a prolonged release phase (Figure S6A).[26] When analyzing the cumulative release of ampicillin with the power-law model (**Equation IX**), it was found that the release kinetics of ampicillin changes from Fickian diffusion control (release

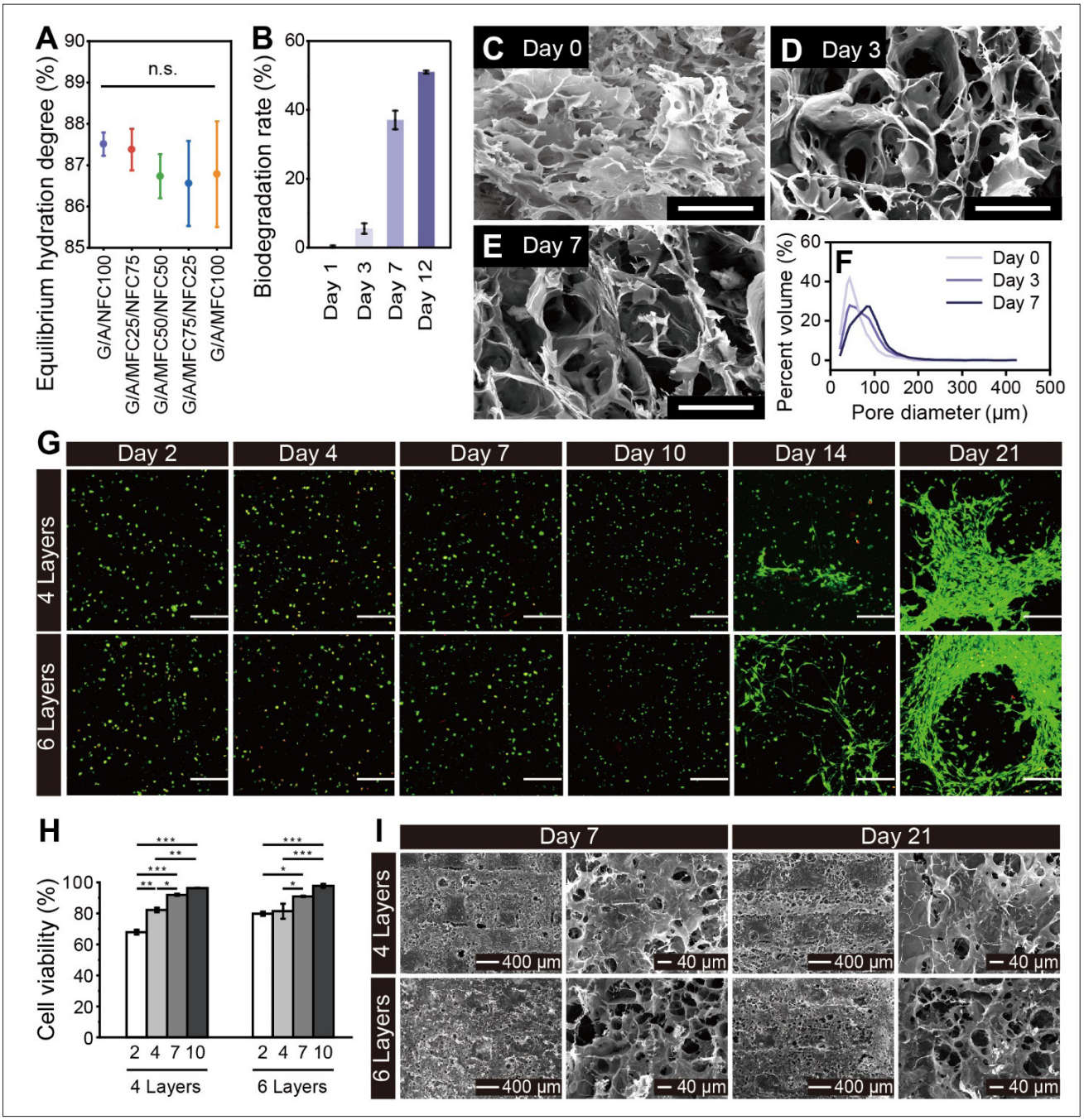

Figure 4. Prolonged biodegradation of G/A/NFC100 hydrogel and cytocompatibility of G/A/NFC100 scaffolds. (A) Equilibrium hydration degree of cellulose-composited G/A ICE hydrogels after 48 h of swelling in deionized water. The size of fibrillated fiber does not have much effect on the water content of the hydrogel. (B) Biodegradation rates of G/A/NFC100 after 1, 3, 7, and 12 days of immersion in 1× dPBS with 5 U/mL collagenase type II. (C–E) Morphologies of G/A/NFC100 hydrogel before biodegradation (C), after 3 days (D), and 7 days of biodegradation (E) by SEM. Scale bar = 100 μm. (F) The pore size distribution of G/A/NFC100 after 0, 3, and 7 days of biodegradation by μCT. (G) Confocal Z-stack images of merged dead and live cells in 4- and 6-layered G/A/NFC100 scaffolds over 21 days. Scale bar = 200 μm. (H) Cell viability in bioprinted G/A/NFC100 scaffolds with 4 and 6 layers after incubation of 2, 4, 7, and 10 days. (I) SEM images of cell-loaded 4- and 6-layered G/A/NFC100 scaffolds after incubation of 7 and 21 days at different magnifications. Abbreviations: dPBS, Dulbecco's phosphate-buffered saline; G/A, Gelatin methacryloyl/alginate; ICE, Ion–covalent entanglement; MFC, Microfibrillated cellulose; μCT, Micro-computed tomography; NFC, Nanofibrillated cellulose; SEM, Scanning electron microscopy.

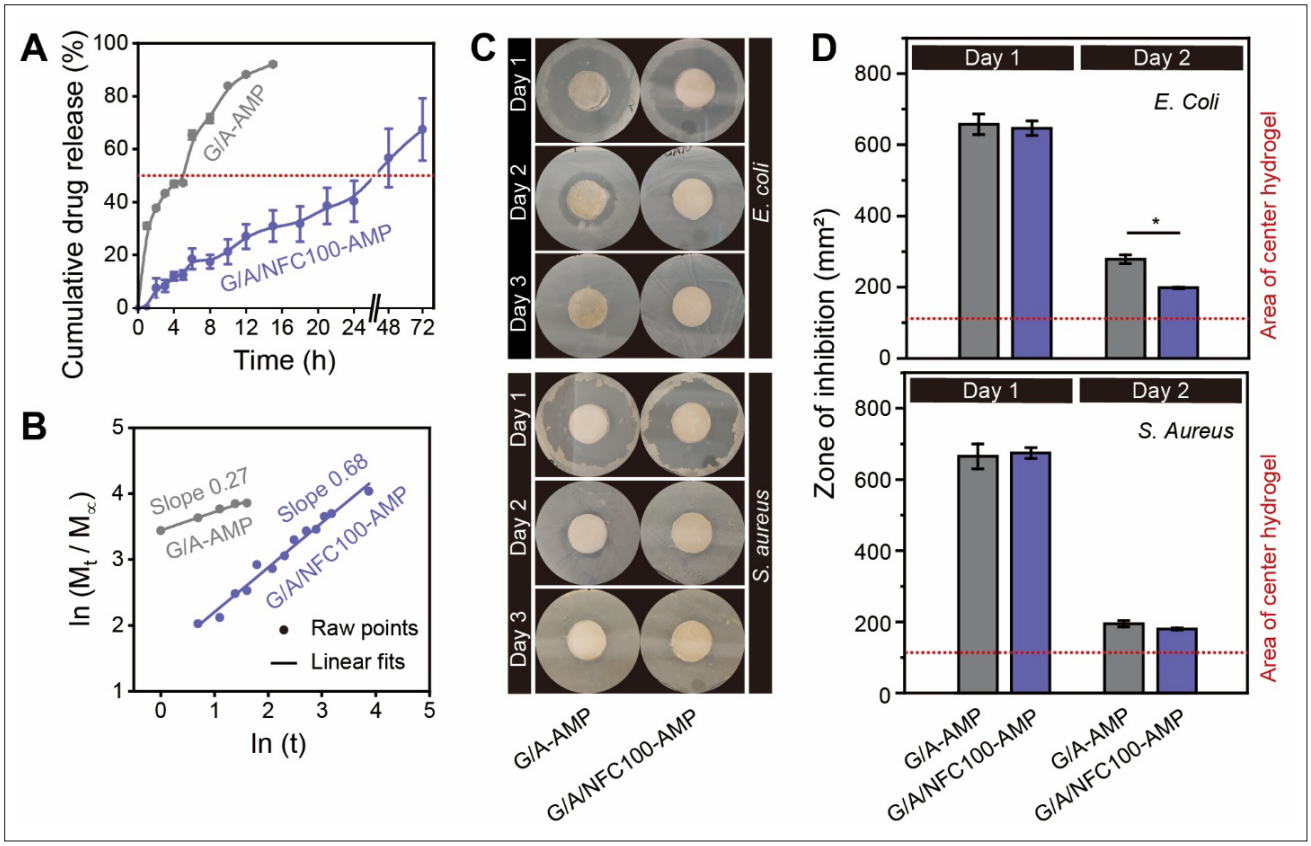

Figure 5. Controlled drug release and antibacterial properties of G/A/NFC100-AMP hydrogels. (A) Representative curves of cumulative drug released from G/A-AMP and G/A/NFC100-AMP hydrogel discs over time. NFC slows down the process of ampicillin release from the hydrogel discs. (B) Linear fits of the first 60% cumulative drug release according to **Equation IX**. The slope of the linear fits represents the release index (n_r), characterizing the drug release mechanism. The addition of NFC changes the ampicillin release mechanism of G/A hydrogel from Fickian diffusion-controlled release to anomalous transport. (C) Antibacterial activities of ampicillin-loaded hydrogels against *E. coli* and *S. aureus* on agar plates after incubating 1, 2, and 3 days. (D) Areas of the inhibition zone for sample G/A-AMP and G/A/NFC100-AMP against *E. coli* and *S. aureus*. Abbreviations: AMP, Ampicillin sodium salt; G/A, Gelatin methacryloyl/alginate; NFC, Nanofibrillated cellulose.

index n_r of 0.27) in G/A-AMP to anomalous transport (n_r of 0.68) in G/A/NFC100-AMP, as demonstrated in Figure 5B. Moreover, the size differences between NFC and MFC do not significantly affect the release kinetics of ampicillin since n_r all fall within the range of 0.45–0.89 (Figure S6B). The above results indicate that the large specific surface area and porous nature of NFC could promote the physical adsorption of ampicillin on NFC,[40] which not only increases drug loading capacity of G/A/NFC100, but also facilitates the long-term slow release of ampicillin in the sample.

Finally, the impact of NFC incorporation on the capacity of ampicillin to execute its own antimicrobial function within the hydrogel was investigated. In Figure 5C and Figure S7, both G/A-AMP and G/A/NFC100-AMP exhibit clear zones of inhibition against *E. coli* and *S. aureus* on the first day. The inhibition zone is significantly reduced on the second day, while only G/A/NFC100-AMP shows a slight zone of inhibition on the third day. When the area of the inhibitory zone was quantified (Figure 5D), no difference in inhibition against *E. coli* and *S. aureus* was observed between the two samples on the first day. However, the inhibition against *E. coli* by G/A-AMP was superior to that of G/A/NFC100-AMP on the second day, which may be related to the rapid release of ampicillin in G/A-AMP. The above results indicate that NFC does not hinder the antimicrobial properties of ampicillin in hydrogels although AMP physically adsorbs on the NFC network.

4. Conclusion

In this work, nanofibrillated cellulose (NFC)-composited G/A formulation (G/A/NFC100) was developed for 3D bioprinting of mouse preosteoblasts MC3T3-E1. The

excellent shear thinning property, recoverability in viscosity and modulus, and gel-like macro fluidity of G/A/NFC100 evidence that it can be successfully extruded to develop 3D scaffolds suitable for tissue reconstruction. Furthermore, the effects of dispensing pressure, print speed, and nozzle size on the accuracy of extruded filaments were investigated, based on which the optimal printing conditions were confirmed. 20-layered crosslinked scaffolds with different geometries were constructed, which showed an excellent mechanical stability. Moreover, MC3T3-E1 encapsulated in printed G/A/NFC100 scaffolds remained consistently high viability throughout the 21 days of incubation, demonstrating the cytocompatibility of G/A/NFC100 scaffolds. The nanofibrillated cellulose was also able to promote the drug loading capacity of G/A hydrogel and the long-term controlled release of ampicillin. Thus, such active and drug-loaded 3D scaffolds are expected to play a role in multifunctional biomedical applications such as tissue regeneration and drug development.

Acknowledgments

The first author would like to thank Dr. David Bassett and Dr. Miruna Chipara in the Healthcare Technologies Institute for their support on her research.

Funding

We thank the financial support provided by the UKRI (Horizon Europe Guarantee scheme, 10066793), and FiberLean Technologies for kindly providing microfibrillated cellulose samples. Z.J.Z. thanks the financial support given by the Engineering and Physical Science Research Council (EP/V029762/1). N.L. acknowledges the Chinese Scholarship Council for the awarded scholarship (CSC201906950042).

Conflict of interest

The authors declare they have no competing interests.

Author contributions

Conceptualization: Na Li, Zhenyu Jason Zhang
Formal analysis: Na Li, Roxana Guillen De La Cruz, Zhenyu Jason Zhang
Investigation: Na Li, LinGe Wang, Zhenyu Jason Zhang
Methodology: Na Li, Roxana Guillen De La Cruz, Zhenyu Jason Zhang
Writing–original draft: Na Li, LinGe Wang, Zhenyu Jason Zhang
Writing–review & editing: All authors

Ethics approval and consent to participate

Not applicable.

Consent for publication

Not applicable.

Availability of data

Data will be made available upon request to the corresponding author.

References

1 Fang Y, Guo Y, Liu T, *et al*. Advances in 3D bioprinting. *Chin J Mech Eng Addit Manuf Front*. 2022;1(1): 100011.
doi: 10.1016/j.cjmeam.2022.100011

2 Zhang B, Gao L, Ma L, Luo Y, Yang H, Cui Z. 3D bioprinting: a novel avenue for manufacturing tissues and organs. *Engineering*. 2019;5(4):777-794.
doi: 10.1016/j.eng.2019.03.009

3 Sharma C, Raza MA, Purohit SD, *et al*. Cellulose-based 3D printing bio-inks for biomedical applications: a review. *Int J Biol Macromol*. 2025;305:141174.
doi: 10.1016/j.ijbiomac.2025.141174

4 Mo Q, Huang L, Sheng Y, *et al*. Crosslinking strategy and promotion role of cellulose as a composite hydrogel component for three-dimensional printing – a review. *Food Hydrocoll*. 2024;154:110079.
doi: 10.1016/j.foodhyd.2024.110079

5 You P, Sun H, Chen H, *et al*. Composite bioink incorporating cell-laden liver decellularized extracellular matrix for bioprinting of scaffolds for bone tissue engineering. *Biomater Adv*. 2024;165:214017.
doi: 10.1016/j.bioadv.2024.214017

6 Ouiyangkul P, Hirun N, Suknuntha K, Tantishaiyakul V. Development and characterization of 3D bioprintable and mechanically reinforced hydrogel based on gellan gum/methylcellulose/cellulose nanocrystals. *Polym Adv Technol*. 2024;35(1):e6206.
doi: 10.1002/pat.6206

7 Suamte L, Tirkey A, Barman J, Jayasekhar Babu P. Various manufacturing methods and ideal properties of scaffolds for tissue engineering applications. *Smart Mater Manuf*. 2023;1:100011.
doi: 10.1016/j.smmf.2022.100011

8 Mohammed A, Jiménez A, Bidare P, *et al*. Review on engineering of bone scaffolds using conventional and additive manufacturing technologies. *3D Print Addit Manuf*. 2023;11(4):1418-1440.

doi: 10.1089/3dp.2022.0360

9 Li N, Guo R, Zhang ZJ. Bioink formulations for bone tissue regeneration. *Front Bioeng Biotechnol*. 2021;9. doi: 10.3389/fbioe.2021.630488

10 Yang J, Wang J, Yang Y, *et al*. 3D-printed bioactive scaffolds: an emerging strategy for the regeneration of infectious bone defects. *Int J Bioprint*. 2024;11(2):79-138. doi: 10.36922/ijb.4986

11 Zhao T, Liu Y, Wu Y, Zhao M, Zhao Y. Controllable and biocompatible 3D bioprinting technology for microorganisms: fundamental, environmental applications and challenges. *Biotechnol Adv*. 2023;69:108243. doi: 10.1016/j.biotechadv.2023.108243

12 Chen A, Wang W, Mao Z, *et al*. Multimaterial 3D and 4D bioprinting of heterogenous constructs for tissue engineering. *Adv Mater*. 2024;36(34):2307686. doi: 10.1002/adma.202307686

13 Liu S, Yu J-M, Gan Y-C, *et al*. Biomimetic natural biomaterials for tissue engineering and regenerative medicine: new biosynthesis methods, recent advances, and emerging applications. *Mil Med Res*. 2023;10(1):16. doi: 10.1186/s40779-023-00448-w

14 Tarsitano M, Ming CLC, Idais D, *et al*. Sericin improves alginate-gelatin hydrogels' mechanical properties, porosity, durability, and viability of fibroblasts in cardiac spheroids. *Int J Bioprint*. 2024;11(1):327-346. doi: doi: 10.36922/ijb.5678

15 Jahani A, Nourbakhsh MS, Ebrahimzadeh MH, Mohammadi M, Yari D, Moradi A. Biomolecules- loading of 3D-printed alginate-based scaffolds for cartilage tissue engineering applications: a review on current status and future prospective. *Arch Bone Jt Surg*. 2024;12(2):92-101. doi: 10.22038/abjs.2023.73275.3396

16 Liu F, Jiang J, Zhe M, Yu P, Xing F, Xiang Z. Alginate-based 3D bioprinting strategies for structure–function integrated tissue regeneration. *J Mater Chem B*. 2025;13(40):12765-12811. doi: 10.1039/D5TB01489A

17 de Souza JR, Rahimnejad M, Mendes Soares IP, *et al*. 3D printing β-TCP-laden GelMA/alginate interpenetrating-polymer-network biomaterial inks for bone tissue engineering. *Bioprinting*. 2025;49:e00413. doi: 10.1016/j.bprint.2025.e00413

18 Aldana AA, Valente F, Dilley R, Doyle B. Development of 3D bioprinted GelMA-alginate hydrogels with tunable mechanical properties. *Bioprinting*. 2021;21:e00105. doi: 10.1016/j.bprint.2020.e00105

19 Seddiqi H, Oliaei E, Honarkar H, *et al*. Cellulose and its derivatives: towards biomedical applications. *Cellulose*. 2021;28(4):1893-1931. doi: 10.1007/s10570-020-03674-w

20 Tabatabaei Hosseini BS, Meadows K, Gabriel V, Hu J, Kim K. Biofabrication of cellulose-based hydrogels for advanced wound healing: a special emphasis on 3D bioprinting. *Macromol Biosci*. 2024;24(5):2300376. doi: 10.1002/mabi.202300376

21 Singh P, Baniasadi H, Gupta S, *et al*. 3D-printed cellulose nanocrystals and gelatin scaffolds with bioactive cues for regenerative medicine: advancing biomedical applications. *Int J Biol Macromol*. 2024;278:134402. doi: 10.1016/j.ijbiomac.2024.134402

22 Jiao H, Shi Y, Sun J, *et al*. Sawdust-derived cellulose nanofibrils with high biosafety for potential bioprinting. *Ind Crops Prod*. 2024;209:118025. doi: 10.1016/j.indcrop.2024.118025

23 Carvalho JPF, Lameirinhas NS, Teixeira MC, *et al*. All-cellulose hydrogel-based bioinks for the versatile 3D bioprinting of different cell lines. *Biomacromolecules*. 2025;26(3):1761-1770. doi: 10.1021/acs.biomac.4c01546

24 Lameirinhas NS, Carvalho JPF, Teixeira MC, *et al*. Nanocomposite hydrogel-based bioinks composed of a fucose-rich polysaccharide and nanocellulose fibers for 3D-bioprinting applications. *Bioprinting*. 2025;45: e00382. doi: 10.1016/j.bprint.2024.e00382

25 Li N, Qi S, Buccoli L, *et al*. Multiscale mechanical properties and enhancement mechanism of cellulose-composited hydrogels. *Carbohydr Polym*. 2025;357:123421. doi: 10.1016/j.carbpol.2025.123421

26 Li N, Bassett DC, Zhang ZJ. Microfibrillated cellulose (MFC)-composite formulations for 3D bioprinting with excellent printability, mechanical strength, and biological functionality. *Chem Eng J*. 2025:169037. doi: 10.1016/j.cej.2025.169037

27 Gatenholm P, Martinez H, Karabulut E, *et al*. Development of nanocellulose-based bioinks for 3D bioprinting of soft tissue. In: Ovsianikov A, Yoo J, Mironov V, eds. *3D Printing and Biofabrication*. New York, NY: Springer International Publishing; 2016:1-23. doi: 10.1007/978-3-319-45444-3_14

28 Webb B, Doyle BJ. Parameter optimization for 3D bioprinting of hydrogels. *Bioprinting*. 2017;8:8-12. doi: 10.1016/j.bprint.2017.09.001

29 Lewicki J, Bergman J, Kerins C, Hermanson O. Optimization of 3D bioprinting of human neuroblastoma cells using sodium alginate hydrogel. *Bioprinting*. 2019;16:e00053. doi: 10.1016/j.bprint.2019.e00053

30 Ouyang L, Yao R, Zhao Y, Sun W. Effect of bioink properties on printability and cell viability for 3D bioplotting of embryonic stem cells. *Biofabrication*. 2016;8(3):035020. doi: 10.1088/1758-5090/8/3/035020

31 Thakur B, Sharma G, Kumar A, *et al*. Designing of bentonite based nanocomposite hydrogel for the adsorptive removal and controlled release of ampicillin. *J Mol Liq*. 2020;319:114166.
doi: 10.1016/j.molliq.2020.114166

32 Ignacio M, Slater GW. Using fitting functions to estimate the diffusion coefficient of drug molecules in diffusion-controlled release systems. *Phys A* 2021;567:125681.
doi: 10.1016/j.physa.2020.125681

33 Ritger PL, Peppas NA. A simple equation for description of solute release I. Fickian and non-fickian release from non-swellable devices in the form of slabs, spheres, cylinders or discs. *J Controlled Release*. 1987;5(1):23-36.
doi: 10.1016/0168-3659(87)90034-4

34 Llabot JM, Manzo RH, Allemandi DA. Drug release from carbomer:carbomer sodium salt matrices with potential use as mucoadhesive drug delivery system. *Int J Pharm*. 2004;276(1):59-66.
doi: 10.1016/j.ijpharm.2004.02.006

35 Karvinen J, Kellomäki M. Design aspects and characterization of hydrogel-based bioinks for extrusion-based bioprinting. *Bioprinting*. 2023;32:e00274.
doi: 10.1016/j.bprint.2023.e00274

36 Hernández-Sosa A, Ramírez-Jiménez RA, Rojo L, *et al*. Optimization of the rheological properties of self-assembled tripeptide/alginate/cellulose hydrogels for 3D printing. *Polymers*. 2022;14(11).
doi: 10.3390/polym14112229

37 Nechyporchuk O, Belgacem MN, Pignon F. Rheological properties of micro-/nanofibrillated cellulose suspensions: wall-slip and shear banding phenomena. *Carbohydr Polym*. 2014;112:432-439.
doi: 10.1016/j.carbpol.2014.05.092

38 Markstedt K, Mantas A, Tournier I, Martínez Ávila H, Hägg D, Gatenholm P. 3D Bioprinting human chondrocytes with nanocellulose–alginate bioink for cartilage tissue engineering applications. *Biomacromolecules*. 2015;16(5):1489-1496.
doi: 10.1021/acs.biomac.5b00188

39 Mogha P, Iyer S, Majumder A. Extracellular matrix protein gelatin provides higher expansion, reduces size heterogeneity, and maintains cell stiffness in a long-term culture of mesenchymal stem cells. *Tissue Cell*. 2023;80:101969.
doi: 10.1016/j.tice.2022.101969

40 El-Samaligy MS, El-Mahrouk GM, El-Kirsh TA. Adsorption—desorption effect of microcrystalline cellulose on ampicillin and amoxycillin. *Int J Pharm*. 1986;31(1):137-144.
doi: 10.1016/0378-5173(86)90223-1